PHYSICAL REVIEW MATERIALS **8**, 015204 (2024)

Chiral symmetry-preserving coupling method for topological acoustic metamaterials

Ssu-Ying Chen[1,*] and Camelia Prodan[1,2,†]

[1] *Department of Physics, New Jersey Institute of Technology, Newark, New Jersey 07102, USA*
[2] *Department of Physics and Engineering Physics, Fordham University, Bronx, New York 10458, USA*

(Received 13 March 2023; accepted 18 December 2023; published 16 January 2024)

Acoustic crystals have emerged as a versatile platform for studying topological phases, showcasing their universality and diversity. The properties of topological insulators and their boundary states depend on the space dimension and symmetries of materials, as evidenced by the periodic table of topological invariants. Studying and observing different topological classes require precise enforcement of topological symmetries and this poses a big challenge for acoustic metamaterials. In this paper, we propose and demonstrate an effective experimental coupling strategy for acoustic crystals, while maintaining the integrity of chiral symmetry. We employed the SSH model for testing purposes to ascertain whether various types of connections support topologically edge and interface modes. We observed that a modular platform, where the resonators are coupled through the bottom, provides support for topologically protected edge and interface states. This platform exhibits exceptional versatility, including reconfigurability, as well as preservation of chiral symmetry.

DOI: 10.1103/PhysRevMaterials.8.015204

I. INTRODUCTION

Topological insulators have attracted significant interest due to their unique characteristics, distinguishing them from both metals and insulators [1]. Recently, there has been a surge of interest in the topological states of bosons, such as photons [2] and phonons [3]. The field of topological materials and metamaterials has opened up new avenues for exploring innovative mechanical and acoustic phenomena. In particular, the realm of topological phononics has emerged as a captivating and promising area of study, offering exciting possibilities for unconventional and unexpected manipulation of sound by harnessing the principles of topology.

Significant advancements have been made in the realm of topological dynamical effects within periodic acoustic systems, with the emergence of phenomena akin to quantum Hall states [4,5], quantum spin-Hall states [6], valley-Hall states [7], and Floquet topological systems [8]. These proposals have been not only theoretically formulated but also experimentally substantiated.

In addition to periodic systems, nonperiodic topological systems have been demonstrated to exhibit topological edge states. This includes topological quasicrystals [9–12], where topological effects arise from incommensurate structural modulations. Further diversifying the field are investigations into different fractal geometries [13–15]. The concept of topological acoustic insulators has introduced innovative possibilities for designing devices with advanced functionalities. Examples include enhancing leaky-wave acoustic antennas [16], developing directional topological acoustic antennas to control sounds for various applications [17], achieving specific signal filtering by introducing controlled disorder into clean structures [18], and exploring various soundproofing strategies [19–21].

In essence, researchers have been fervently exploring diverse topological acoustic systems, with particular emphasis on topological acoustic metamaterials composed of numerous phononic crystals as a focal point.

Topological insulators, often referred to as symmetry-protected topological phases of matter, are characterized by their gapped phases with topological properties that hinge upon specific symmetries. This unique attribute is a consequence of the global characteristics of the topological insulator's band structure: Local disturbances cannot disrupt or damage its surface state. Given that the attributes of topological insulators and their surface states are closely linked to the material's dimension and symmetries, they can be systematically classified using the periodic table of topological insulators [22]. From an experimental perspective, it is essential to adhere to specific structures and symmetries, as maintaining symmetry is equivalent to preserving topological properties. To accomplish this, coupling methods must be carefully chosen for topological acoustic experiments. This leads to a pertinent question: In periodic acoustic resonant models, how can resonators be efficiently coupled to achieve desired structures while preserving symmetry, thus aligning with the concept of topological metamaterials?

Symmetry preservation methods often employ a double-sided connection approach, where an additional coupling bridge is added to the side, rendering the structure symmetric [23–26]. However, this approach necessitates the 3D printing of resonators using photosensitive resins or other materials for the coupling bridges, adding complexity and time to the manufacturing process. Furthermore, any adjustments to the dimensions of the coupling bridge require starting the entire manufacturing process anew.

In this article, we study acoustic coupling and present an a method that connects resonators through the bottom to

---

[*] sc945@njit.edu

[†] cprodan@fordham.edu

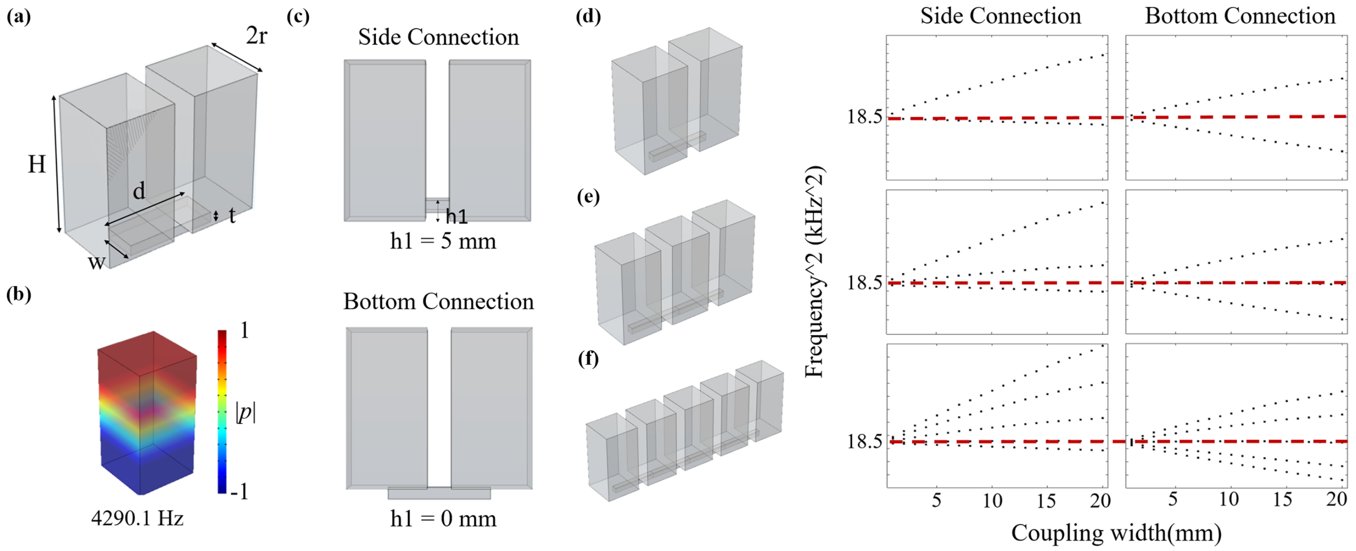

FIG. 1. Simulations showing that the bottom connection preserves the symmetry. (a) Dimensions of the resonators and coupling bridges. $H = 40$ mm, $r = 10$ mm. The coupling bridge has a width = 5 mm, length $d = 26$ mm, thickness $t = 3$ mm. (b) The acoustic pressure distributions of the eigenmode (the first mode) under investigation. Red color represents air expansion, while blue color represents air contraction. (c) Height position of the coupling bridge: $h1 = 5$ mm for side connection, $h1 = 0$ mm for bottom connection. (d) Dimer structure and the band spectrum for both side and bottom coupling methods. (e) Trimer structure and the band spectrum for both side and bottom coupling methods. (f) Pentamer structure and the band spectrum for both side and bottom coupling methods. In the band spectrum of all three cases, it is clear that symmetry is maintained when the resonators are connected through the bottom. Red dashed lines indicate the symmetrical axis.

preserve symmetry and establish a straightforward, adaptable platform akin to Lego building blocks. To examine the topological symmetry, we leverage the existence of chiral symmetry in the phonon spectrum as a means to validate the topological robustness of our design. The chiral symmetry of a Hamiltonian is mirrored in its spectrum. For every energy state E, a corresponding chiral symmetric state exists with energy $-E$ [27]. Regarding the phonon spectrum, this implies that each resonant mode possesses an energy-wise symmetric counterpart. The original resonant frequency serves as the axis of symmetry. Throughout the paper, we conduct a comparative analysis between two coupling methods: Side coupling and bottom coupling [Fig. 1(c)]. Our investigation commences with a demonstration of how bottom coupling effectively preserves symmetry in simple periodic acoustic models, while single side coupling falls short in this regard. We employ simulations to analyze the resonant modes of various structures, including dimers, trimers, pentamers, and classic Su-Schrieffer-Heeger (SSH) models consisting of 14 and 28 resonators, the latter with a domain boundary. Additionally, we present experimental results for the dimer, the SSH model, and the SSH model with a domain boundary. These experimental findings consistently align with the simulations, highlighting the efficiency and simplicity of the bottom coupling method.

II. RESULTS and DISCUSSION

The dimensions of the resonators employed in both simulations and experiments are illustrated in Figs. 1(a) and 1(c).

A. Side Connection vs. Bottom Connection

To compare the effect of side connection versus bottom connection for topological acoustic crystals, numerical simulations were done using COMSOL Multiphysics software.

The simulated results are reported in Fig. 1, showcasing dimer, trimer, and pentamer resonator structures with both side bridge coupling and bottom bridge coupling [Fig. 1(c)]. The band spectra [Figs. 1(d), 1(e), 1(f)] were generated by systematically varying the width of the coupling bridge from 1 mm to 20 mm in 1 mm increments and plotting the corresponding eigenfrequencies against the bridge widths. A wider coupling bridge corresponds to a stronger coupling strength. Notably, in the band spectrum, the second mode splits and the gap widens as the coupling strength increases. When symmetry axes are denoted by red dashed lines, it becomes evident that with side connection, the splitting modes lack symmetry. However, relocating the coupling bridges to the bottom restores symmetry.

B. Dimer experiment

Prior to beginning experiments, we conducted a simulation to determine the most suitable resonator height, as indicated by the red star in the Fig. 2(a). Our investigations led us to conclude that a resonator height of 40 mm is optimal for our purposes. In order to eliminate any potential interference stemming from the speaker's resonant frequency, we undertook a blank test that involved only the speaker and microphone. We positioned the microphone directly facing the speaker, maintaining a separation of about 5 mm. Through this approach, we identified the optimal frequency range for

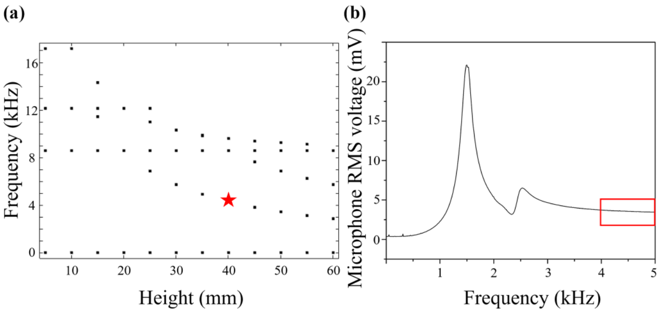

FIG. 2. Preliminary tests conducted prior to the experiment to ensure seamless operation. (a) The height of a resonator was swept from 1 mm to 60 mm using COMSOL to identify the most suitable height value. Given our emphasis on the first longitudinal modes and the necessity to avoid microphone resonant frequencies, we determined the optimal height to be 40 mm, indicated by the red star. (b) A blank test was performed to establish the frequency measurement range. The peak at 1500 Hz corresponds to the self-resonant frequency of the microphone.

our specific experiment, which is between 4 KHz and 5 KHz, as highlighted by the red box in Fig. 2(b).

To investigate any potential leakage between the resonators and the base, we performed a leakage test in addition to our standard dimer measurements [Fig. 3(f)]. During the leakage test, the microphone was positioned adjacent to the junction where the resonator and base meet, following the positions illustrated in the figure in the red box. The results, as depicted in the right panel of Fig. 3(f), indicate that the signal obtained from the junction of resonator and the base is significantly lower in comparison to the dimer measurement. Based on the conclusive outcomes of these tests, we can assert that any potential leakage can be disregarded.

We conducted an experimental validation of the dimer coupling to corroborate the simulation findings. In Fig. 3(e), we display the COMSOL-simulated acoustic pressure fields of the resonant modes, where the coupling width was set to 5 mm. The assembly process is outlined in Figs. 3(a) and 3(b), while the experimental setup is depicted in Fig. 3(f), left panel. Both the speaker and microphone were positioned atop the same resonator for sound emission and collection, respectively. The input signal sent to the speaker ranged from 4 kHz to 5 kHz, with 10 Hz intervals. The experimental results for the dimer with bottom coupling bridges closely match the simulations [Fig. 3(c), bottom panel]. Notably, the midpoint between the two peaks is approximately 4.3 kHz, coinciding with the point where the two modes commence splitting in the band spectrum (around 18.5 kHz^2). Conversely, when employing side connection, the peak positions deviated from the spectrum. Moreover, the difference in peak heights is noticeably smaller for bottom coupling than for side coupling [Fig. 3(d)]. Comparing these outcomes with those obtained through the bottom coupling method, it becomes evident that symmetry is markedly absent in the case of side coupling.

C. SSH acoustic model

To gain a deeper understanding of how the positioning of connections within acoustic crystals affects the topological gaps in the band spectrum, we initiated simulations involving three connection types for an SSH model comprising 14 resonators. The first type involved coupling them with bridges connected through the side, the second utilized double side coupling bridges, and the third employed bottom connection. Figure 4(a) provides a top view of the SSH coupling bridges, where r_1 and r_2 represent the widths of the coupling bridges, making them crucial for determining the alternating coupling strength. Light blue dashed lines indicate the locations of the resonators. The geometries of the three coupling types are presented in Figs. 4(b), 4(c), 4(d). We generated the resonant spectrum by sweeping S, which represents half of the difference in widths between strong and weak coupling bridges, from -9 mm to 9 mm. When S equals zero, all coupling bridges share a uniform width of 10 mm.

In the spectrum [Figs. 4(b), 4(c), 4(d)], it is evident that there is no distinct gap when using a uniform coupling connection ($S = 0$ mm, $r_1 = r_2 = 10$ mm). In the current configuration with only 14 resonators, it is important to note that this seemingly gap is a result of the limited number of resonators used. By increasing the number of resonators, we can expect a more uniform distribution of modes, which would eliminate the gap. However, a bulk spectral gap becomes evident when the connecting channels feature alternating strong and weak coupling strengths ($S \neq 0$). Moreover, the bulk spectrum maintains its symmetry with respect to the midpoint of the bulk spectral gap, with slight deviations of less than 5% when compared to the overall width of the bulk spectrum.

In Fig. 4(b), in the SSH model with bottom connection, one can readily discern the anticipated edge resonant modes. These modes have their energies concentrated precisely in the center of the bulk spectral gap, which occurs around 18.5 kHz^2, coinciding with the resonant frequency of the second mode in a single resonator. It is safe to assert that the SSH model with bottom connection, as demonstrated in COMSOL-simulated spectra, exhibits a precise chiral symmetry. In Fig. 4(c), the SSH model with double side coupling bridges produces identical spectra, indicating that both coupling approaches successfully preserve chiral symmetry. Conversely, the spectra of the SSH model connected through the sides do not exhibit the same symmetry. In Fig. 4(d), not only do the bands merge into lower bulk bands, giving rise to extended modes, but the midpoint of the spectrum shifts to approximately 2 kHz^2, mirroring the same impracticality observed in the dimer experiments.

We also examined whether the vertical position [$h1$ in Fig. 1(c)] of side coupling influences symmetry preservation. The height of side coupling bridge was swept from bottom to top to generate the spectra in Fig. 4(e), while the coupling width was fixed at $r_1 = 15$ and $r_2 = 5$ ($S = -5$ mm). When $h1$ is set to -21.5 mm or 21.5 mm, the resonators are coupled either from the bottom or the top, resulting in bulk modes that are symmetric with respect to 18.5 kHz^2, with edge modes appearing in the middle. The red sections of the spectra indicate cases where the coupling bridges protrude from either the bottom or the top, meaning that a portion of them is outside the resonators. In these instances, edge modes persist within the gap, but the symmetry gradually shifts away from the dashed line. It is apparent that once the coupling bridges penetrate the

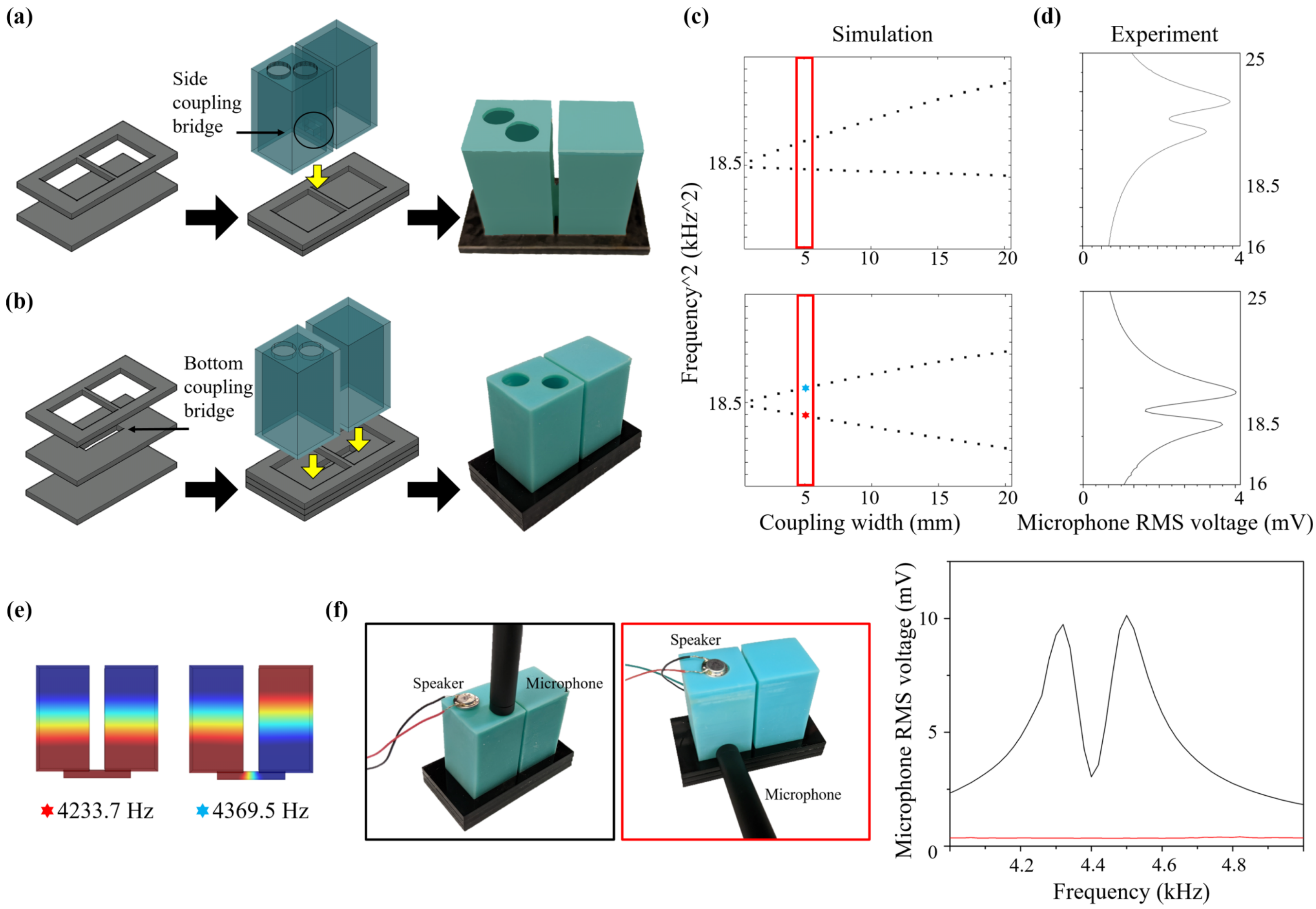

FIG. 3. Dimer experimental setups as well as the comparison of simulation and experiment results. (a) Assembly process of dimer connected through side. The dimer was 3D printed together with a side coupling bridge; the height position of the top of the side coupling bridge $h1$ is equal to 7 mm. (b) Assembly process of dimer connected through bottom. Two resonators were 3D printed separately, and the bottom coupling bridge is grooved in the middle acrylic sheet as depicted. (c) Simulation results of dimers with side connection (top panel) and bottom connection (bottom panel). Red boxes in both band spectrums indicate the coupling width (5 mm) used in the experiment. (d) Experimental results of dimers with side connection (top panel) and bottom connection (bottom panel). (e) Acoustic pressure fields of two split modes of the first mode. (f) The picture within the black box represents our standard measurement setup, while the setup within the red box is designated for conducting the leakage test, to make sure there is no sound leakage in this modular design. The outcomes of these two setups are depicted in the right panel, indicated by the black and red lines.

body of the resonators, the edge modes merge into the bulk, and symmetry dissipates.

Subsequently, we conducted experiments with the SSH model connected through the bottom to ascertain whether the observed symmetry also manifests in the experimental results. Figure 5(a) illustrates the setup employed in the experiments. The COMSOL-simulated acoustic pressure fields of the edge resonant modes are depicted in Fig. 5(b). For reference, we have included the simulated band structure from Fig. 4(b) in Fig. 5(c).

In these measurements, similar to the dimer experiments, we used a setup where both the speaker and the microphone were inserted into the same resonator through two holes located at the top. The speaker's frequency was scanned from 4 kHz to 5 kHz in 20 Hz steps, and the microphone recorded the corresponding signals. This measurement process was repeated for all resonators, and the collected data were compiled to create the local density of states plot depicted in Fig. 5(d). It is noteworthy that all the resonators are designed to be removable and interchangeable. This flexibility allows us to position the resonator with holes at any desired probe location for measurements. Panel (e) offers an alternative representation of the same data. In this depiction, the spectral gap, along with the anticipated edge and interface modes, can be easily seen, and they align closely with the simulations shown in panel (c). The density of states reported in Fig. 5(d) was obtained by integrating the local density of states acquired from resonators corresponding to the probe's position index.

Finally, we conducted a test and comparison of two coupling methods in an SSH model featuring a domain boundary (interface), both through simulations and experiments. At one end of the boundary, known as the nontrivial end or topological end, resides a region with topological characteristics. At the other end, referred to as the trivial end or nontopological end, the region lacks these topological properties. It is shown in Fig. 6(a) where $r_1 = 15$ mm and $r_2 = 5$ mm. The band spectra for side connection and bottom connection are presented in Fig. 6(b) and Fig. 6(c), respectively. Red vertical

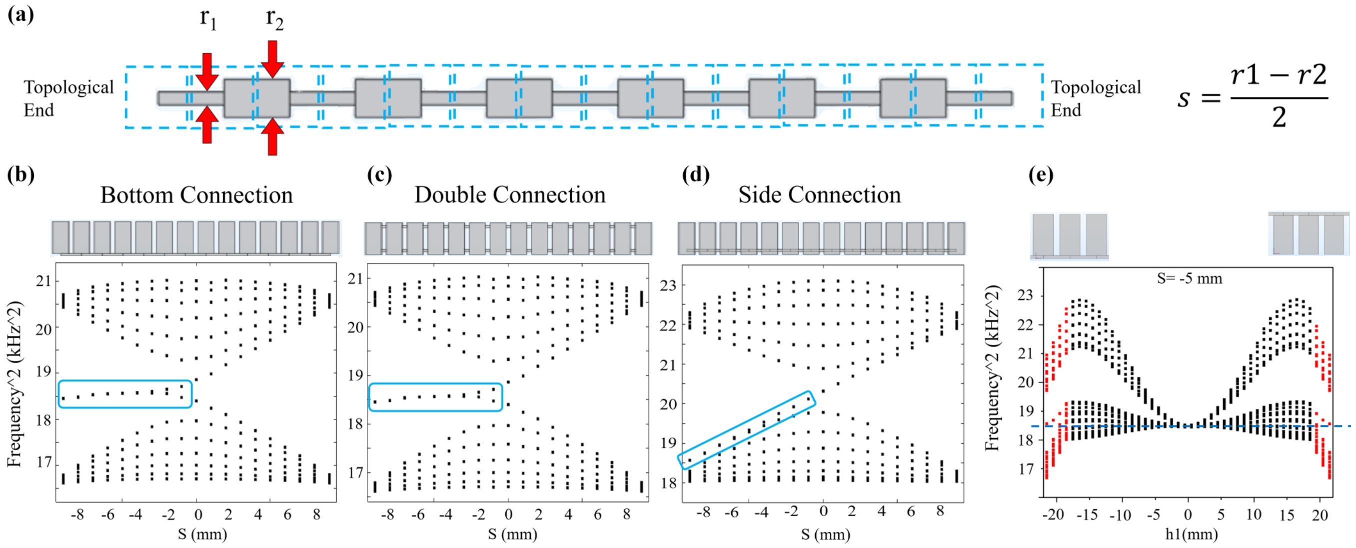

FIG. 4. Band spectrum of different types of connection in SSH model of 14 resonators, sweeping *S*. *S* is half of the difference in widths between strong and weak coupling bridge. (a) Top view of SSH coupling bridges. r_1 and r_2 are related to the alternate coupling strength. Light blue dashed lines are where the resonators were placed. (b) SSH model with bottom connection. (c) SSH model with double connection from the sides. (b) and (c) have very similar spectrum. Blue boxes include edge resonant modes. (d) SSH model with side connection; the band merges into bulk and the modes are no longer edge modes. (e) Band spectrum of SSH model sweeping the height of the coupling bridges. Red parts represent when the coupling bridges protrude from the bottom or top. Dark blue dashed line marks 18.5 kHz^2.

boxes encompass resonant modes when $S = -5$ mm. Red and blue stars denote the positions where interface mode and edge modes emerge, and their corresponding acoustic pressure field maps are displayed below.

Consistent with the previous findings, both simulation and experimentation with bottom coupling confirmed that the system harbors topological resonant modes at the nontrivial edge and the domain boundary, as anticipated. These modes are situated in the middle of the bulk band gap. In contrast, with side coupling, the edge mode vanishes, and the interface mode is located near the bulk. Moreover, it is noticeable that the energy is not as concentrated at the interface, as observed from the distribution of the acoustic pressure field.

We also conducted experiments on the SSH model with bottom connection and a domain boundary, following the same protocol as before. The frequency sweep ranged from

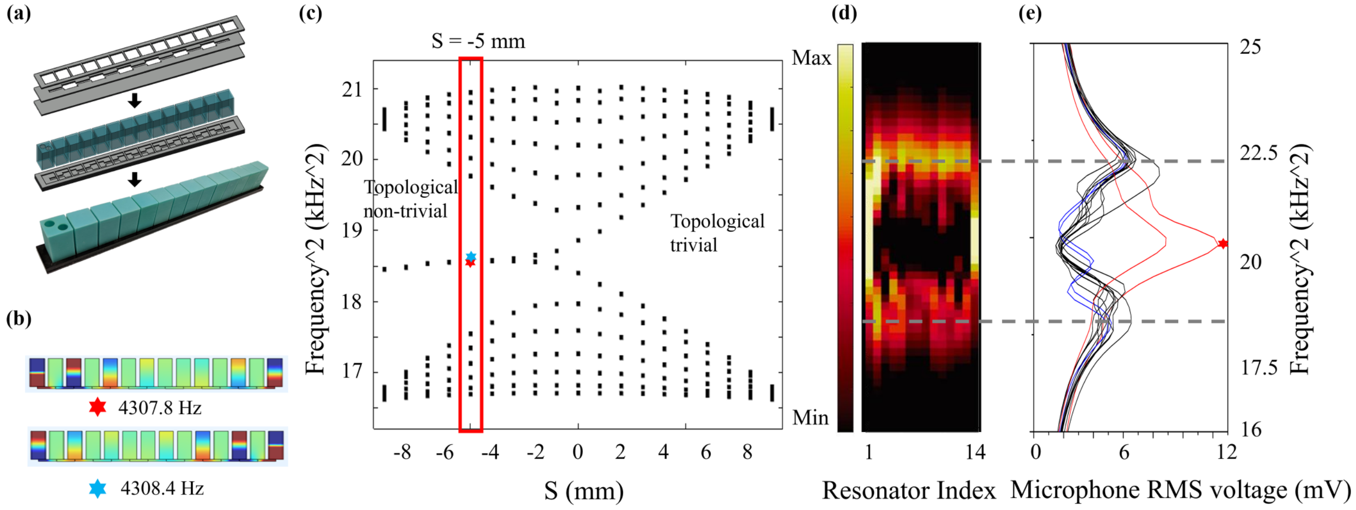

FIG. 5. SSH experiments demonstrate the simplicity and efficiency of bottom coupling method. (a) The assembling process of SSH model of 14 resonators connected through bottom. (b) Acoustic pressure field distribution for the edge modes marked as red and blue dots in panel (c) when $S = -5$ mm. (c) COMSOL-simulated SSH model resonant spectrum. The red vertical box indicates $S = -5$ mm which makes $r_1 = 15$ mm and $r_2 = 5$ mm, the parameters that were used in the experiments. (d) Experimentally measured local density of states, assembled from normalized microphone readings from the top of the block resonators. The bright dispersive modes indicates the bulk and edge modes. (e) Collapse on the frequency axis of the intensity plot in (d). The spectral gap is clearly recognized and the edge modes that show up in the gap are marked with a red star.

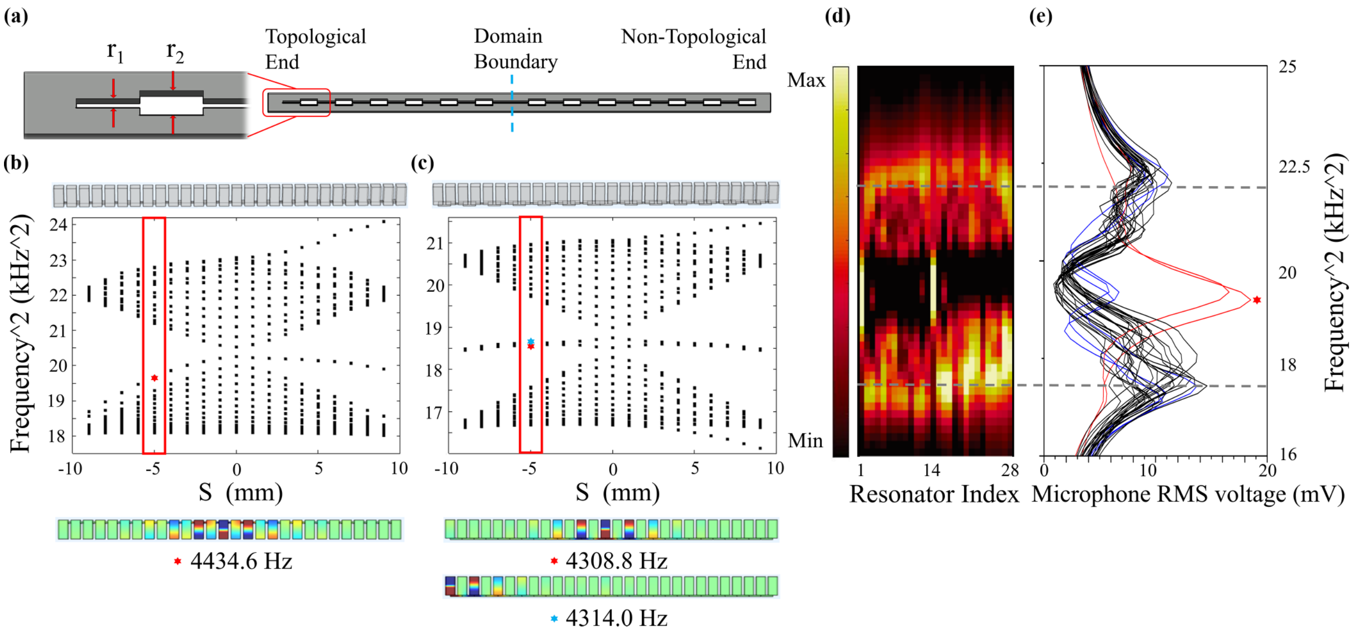

FIG. 6. The SSH model consists of 28 resonators with a domain boundary in the middle, topologically nontrivial at one end and trivial at the other. (a) Coupling bridges and its dimension. $r_1 = 5$ mm and $r_2 = 15$ mm. (b) SSH model with side connection. The acoustic pressure field map below shows the interface mode at the red star in the spectrum when $S = -5$ mm. The model lacks edge modes. (c) SSH model with bottom connection. Band structure and acoustic pressure field maps of both edge mode and interface mode. Blue and red stars in the panel mark edge mode and interface mode, respectively. (d) Experimentally measured local density of states, assembled from normalized microphone readings from the top of the block resonators. The bright dispersive modes indicate the bulk and edge modes. (e) Collapse on the frequency axis of the intensity plot in (d). The spectral gap can be clearly identified and the edge and interface modes show up in the gap marked with a red star.

4 kHz to 5 kHz, and the measurements were systematically repeated for all 28 resonators. The collected data were then utilized to construct the local density of states, as depicted in Fig. 6(d). Panel (e) presents the data from panel (d), collapsed on the frequency axis. The spectral gap, along with the anticipated edge modes, is distinctly discernible and aligns well with the simulations shown in panel (c). Additionally, the COMSOL-simulated acoustic pressure field maps of the edge resonant modes are provided in Figs. 6(b) and 6(c).

D. Decay length analysis

The experimental and simulation-based determination of the decay length was conducted for a SSH model of 14 resonators. The experimental setup was devised, wherein the speaker was positioned and fixed at the the first resonator. Next, microphone responses were sequentially measured from the first to the final resonator. The outcomes are illustrated in Fig. 7(a). By extracting data points at 4400 Hz from the 1st, 3rd, 5th, 7th, 9th, 11th, and 13th resonators, and then using the general expression of exponential decay which is shown below, we applied exponential fitting to determine a decay length of 50.16 ± 2.26 mm [as shown in Fig. 7(b)]:

$$V = V_0 e^{\frac{x}{L}}.$$

Computationally we obtain a similar decay length as experimentally as presented below. Using COMSOL for $s = -5$ ($r_1 = 5$ mm, $r_2 = 15$ mm) and frequency the frequency of the edge mode of = 4308 Hz, we assessed the sound pressure in decibels on the upper surfaces of the 1st, 3rd, 5th, 7th, 9th, 11th, and 13th resonators. Building upon the earlier expression of the decay length and the relationship between sound pressure (SP) and voltage v,

$$\mathrm{SP}(dB) = 20\log\frac{V}{V_0}.$$

Linear regression yielded a decay length of 50.59 ± 0.83 mm from the slope, which is similar with experimental data [Fig. 7(c)].

E. Perturbations introduce by side couplings

Figure 4(e), shows that the coupling bridge diminishes the symmetry pointing to the fact that side coupling could have an impact on the acoustic fields within the resonators. Using the chiral operator $\hat{\Gamma}$, we can write the general expression down [27]:

$$\hat{H}|\psi_n\rangle = E_n|\psi_n\rangle \Rightarrow$$

$$\hat{H}\hat{\Gamma}|\psi_n\rangle = -\hat{\Gamma}\hat{H}|\psi_n\rangle = -\hat{\Gamma}E_n|\psi_n\rangle = -E_n\hat{\Gamma}|\psi_n\rangle.$$

The introduction of side couplings can potentially result in alternating on-site perturbations $\delta E_n|n\rangle\langle n|$ which break the chiral symmetry. The bottom coupling makes all δE_n's equal, hence restores the symmetry. These perturbations can make the resonator seem shorter. Thus, using COMSOL simulations, we conducted a comprehensive study by parametrically sweeping the width of the coupling bridge and of the res-

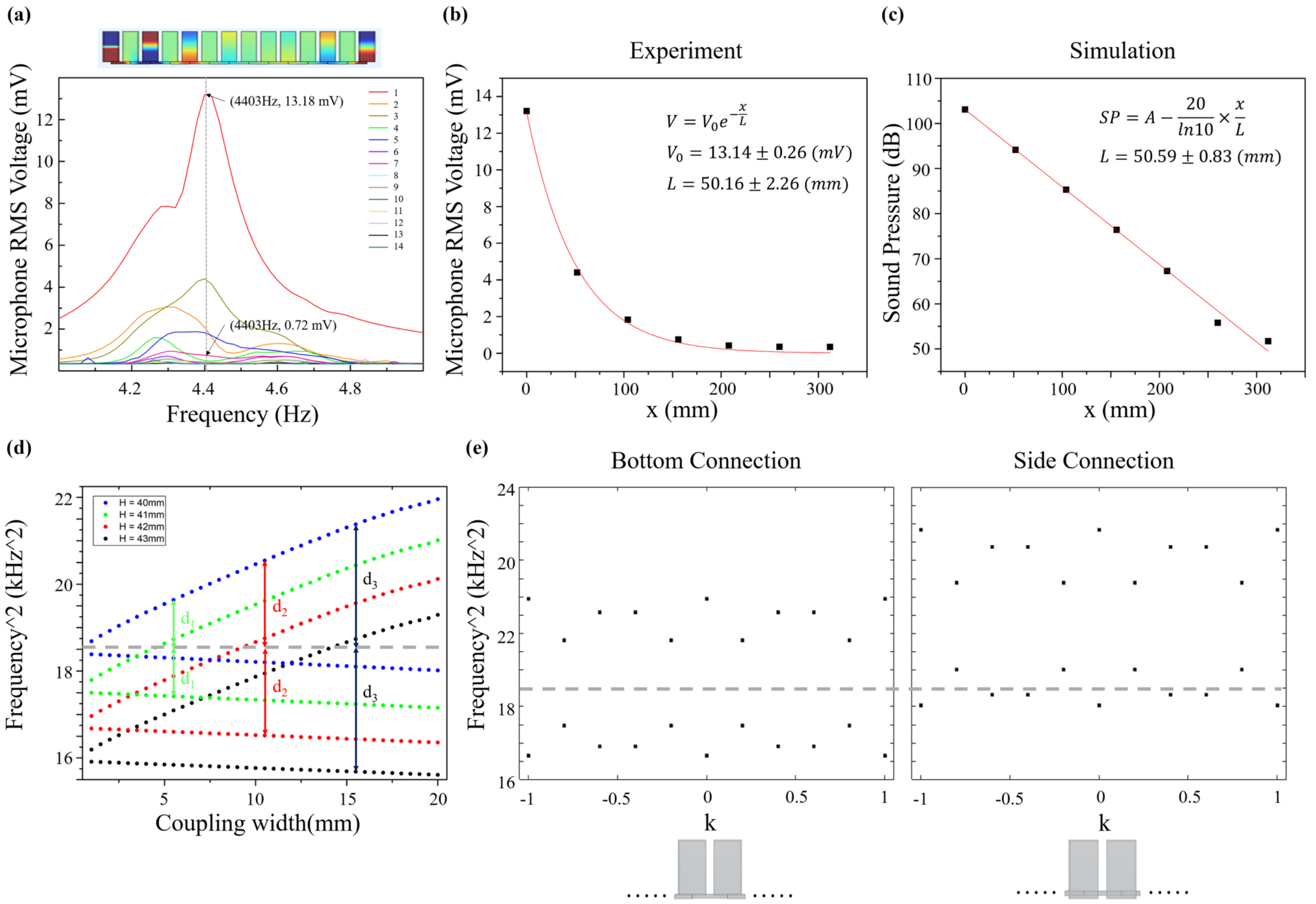

FIG. 7. Side coupling perturbation and decay length analysis. (a) Decay length measurements. The source speaker was placed at the the first resonator, and then the microphone responses were measured sequentially, from the first to the 14th resonator. (b) From (a), data points were extracted at 4400 Hz from the 1st, 3rd, 5th, 7th, 9th, 11th, and 13th resonators; we applied exponential fitting to determine a decay length of 50.16 ± 2.26 mm. (c) Using COMSOL, at $s = -5$ ($r_1 = 5$ mm, $r_2 = 15$ mm) and frequency = 4308 Hz, we evaluated the sound pressure in decibels on the upper surfaces of the 1st, 3rd, 5th, 7th, 9th, 11th, and 13th resonators. Linear fitting yielded a decay length of 25.32 ± 0.42 mm. (d) Side connection perturbs the acoustic fields inside resonators, especially at the bottom, close to the coupling bridge. This way the resonators behave as having a different height. For each resonator height (40, 41, 42, 43) we used COMSOL to sweep the coupling width that would give us the symmetry in energy (frequency square) about the base line of the unperturbed (bottom coupling) resonators. (e) Floquet periodic boundary condition. Intrinsic symmetry in bottom coupling. Gray line indicates the original resonant mode, which is the axis of symmetry.

onators heights: Blue corresponds to the original height of 40 mm, green to 41 mm, red to 42 mm, and black to 43 mm, as depicted in Fig. 7(d). Our investigation aimed to achieve energy symmetry with respect to the baseline established by the 40 mm resonator. For instance, by adjusting the resonator's height to 41 mm, with a bridge width of 6 mm, we were able to locate a mode that shows energy-wise symmetry with the mode observed in the 40 mm resonator. These results show that with side coupling the resonators behave as having different heights. This is true only when we work with only one mode at a time, as is the case of this paper. When multiple modes are present in acoustic measurements the extended analysis presented in [28] should be used.

F. Intrinsic symmetry in bottom coupling

We conducted a simulation using Floquet periodic boundary conditions with an s value of -5 (where $r_1 = 5$ mm and $r_2 = 15$ mm). The unit cells of two coupling methods are shown at the bottom of Fig. 7(e). If we set $kx = \frac{k\pi}{L_x}$, L_x is the total length in the x direction, we can get phonon spectra by sweeping k over the first Brillouin zone $[-\frac{\pi}{L_x}, \frac{\pi}{L_x}]$ [Fig. 7(e)]. In the case of bottom coupling, the band structure as a function of the k vector is symmetric, whereas in the side coupling case, it is asymmetric.

III. CONCLUSION

In this study, we investigated in detail two different acoustic coupling strategies, side coupling and bottom coupling, through a combination of COMSOL simulations and experimental setups. We conducted tests on dimers, single SSH setups, and SSH model with an interface to evaluate the effectiveness of both coupling methods. Coupling through the side required an additional connection to preserve chiral simetry and was more complex in terms of fabrication and implementation. Our findings emphasize the advantages of utilizing a modular setup with coupling through the bottom for preserving symmetries in acoustic systems. The nature of our experimental setup enables the individual printing of resonators and quick assembly of coupling bridges through laser cutting. A decay length of around 50 mm was obtained both experimentally and computationally, showing that the edge mode (or its energy) can be contained within a few resonators even in acoustic systems which is useful in applications where energy storage is targeted. The pressure simulations of the topological or interface edge mode show the well known pattern: Every other resonator has zero pressure (green color), and the pressure flips from low to high every other resonator where pressure exists. The topological edge mode is also localized in the middle of the band gap, another useful application for energy storage, when leaking (or loosing) energy into the bulk (materials) is not desired. Our analysis implies that single side coupling perturbs the acoustic field within the resonators, making it behave as having another length. The bottom coupling is insensitive to such pertubations. This modular platform offers exceptional flexibility, as the resonators can be stored and reused for future experiments, offering convenience and cost effectiveness, and making it a promising strategy for future investigations in the field of acoustic metamaterials.

IV. MATERIAL AND METHODS

A. Simulation

The simulations reported in all figures were performed with the COMSOL Multiphysics pressure acoustic module. The wave propagation domain, as depicted in Fig. 1, was filled with air featuring a mass density 1.3 $\mathrm{kg/m^3}$, and the speed of sound was set to 343 m/s, suitable for room temperature conditions. We treated the 3D printing UV resin material as a hard boundary due to its significant acoustic impedance mismatch when compared to air.

B. Experiment

The resonators were fabricated through 3D printing using an Anycubic Photon 3D printer, using UV resin with an *XY* resolution of 47 μm and a *Z* resolution of 10 μm. The resonator walls have a thickness of 2 mm, a design choice that guarantees a high *Q* factor and validates the use of rigid boundaries in the simulations. The inner dimensions of the resonators are depicted in Fig. 1(a).

A dimer with side coupling bridges was fabricated as a single 3D-printed unit. The dimensions and position of the coupling bridge are indicated in Fig. 1(a). One side of the dimer was left open for ethanol rinsing and UV curing. Subsequently, we placed the dimer on a base comprised of two layers of acrylic plates (the top layer being 2 mm thick, and the bottom layer 3 mm thick) to create an enclosed space for wave propagation [Fig. 3(a)]. The choice of a 2 mm top layer thickness accommodates the side bridge. For the bottom connection, we assembled a supporting base consisting of three layers of 3 mm thick acrylic plates [Fig. 3(b)]. The middle layer includes a groove to facilitate acoustic coupling. The acrylic plates with the supporting base patterns were precisely cut using the Boss Laser-1630 Laser Engraver, with a nominal tolerance of 250 μm.

The same approach was employed for the SSH model connected from the bottom. 14 resonators were positioned and coupled through channels with alternating widths that were grooved into the acrylic plates of the base. These resonators are designed to be detachable and interchangeable, allowing for flexibility in their arrangement. Consequently, acoustic crystals with various probe positions can be configured, and the resonators can be disassembled, stored, and reassembled for future projects or designs.

The protocol for conducting the acoustic measurements presented in Fig. 3, Fig. 5, and Fig. 6 was as follows: Sinusoidal signals with a duration of 1 s and an amplitude of 0.5 V, generated by a Rigol DG 1022 function generator, were transmitted to a speaker positioned within an opening on top of a resonator. A dbx RTA-M Reference Microphone equipped with Phantom Power was placed in an adjacent opening and utilized to capture the acoustic signals [Fig. 3(c)]. Thereafter, the signals were processed by a custom LabVIEW code through a National Instruments USB-6122 data acquisition device, and the data were stored for subsequent graphical representations.

ACKNOWLEDGMENT

The authors acknowledge support from the National Science Foundation, Grant No. CMMI-2131759.

---

[1] M. Z. Hasan and C. L. Kane, Colloquium: Topological insulators, Rev. Mod. Phys. **82**, 3045 (2010).

[2] T. Ozawa *et al.*, Topological photonics, Rev. Mod. Phys. **91**, 015006 (2019).

[3] X. Zhang *et al.*, Topological sound, Phys. Commun. **27**, 1 (2018).

[4] A. Khanikaev, R. Fleury, S. Mousavi *et al.*, Topologically robust sound propagation in an angular-momentum-biased graphene-like resonator lattice, Nat. Commun. **6**, 8260 (2015).

[5] Z. Yang, F. Gao, X. Shi, X. Lin, Z. Gao, Y. Chong, and B. Zhang, Topological acoustics, Phys. Rev. Lett. **114**, 114301 (2015).

[6] C. He, X. Ni, H. Ge *et al.*, Acoustic topological insulator and robust one-way sound transport, Nat. Phys. **12**, 1124 (2016).

[7] J. Lu, C. Qiu, M. Ke, and Z. Liu, Valley vortex states in sonic crystals, Phys. Rev. Lett. **116**, 093901 (2016).

[8] Y. G. Peng, C. Z. Qin, D. G. Zhao, Y.-X. Shen, X.-Y. Xu, M. Bao, H. Jia, and X.-F. Zhu, Experimental demonstration of anomalous Floquet topological insulator for sound, Nat. Commun. **7**, 13368 (2016).

[9] X. Ni, K. Chen, M. Weiner *et al.*, Observation of Hofstadter butterfly and topological edge states in reconfigurable quasi-periodic acoustic crystals, Commun. Phys. **2**, 55 (2019).

[10] W. Cheng, E. Prodan, C. Prodan, Experimental demonstration of dynamic topological pumping across incommensurate bilayered acoustic metamaterials, Phys. Rev. Lett. **125**, 224301 (2020).

[11] D. J. Apigo, W. Cheng, K. F. Dobiszewski, E. Prodan, and C. Prodan, Observation of topological edge modes in a quasiperiodic acoustic waveguide, Phys. Rev. Lett. **122**, 095501 (2019).

[12] A. Coutant, A. Sivadon, L. Zheng, V. Achilleos, O. Richoux, G. Theocharis, and V. Pagneux, Acoustic Su-Schrieffer-Heeger lattice: Direct mapping of acoustic waveguides to the Su-Schrieffer-Heeger model, Phys. Rev. B **103**, 224309 (2021).

[13] G. Song, B. Huang, H. Dong *et al.*, Broadband focusing acoustic lens based on fractal metamaterials, Sci. Rep. **6**, 35929 (2016).

[14] X. Zhao, G. Liu, C. Zhang *et al.*, Fractal acoustic metamaterials for transformer noise reduction, Appl. Phys. Lett. **113**, 074101 (2018).

[15] S. K. Singh, O. Prakash, and S. Bhattacharya, Hybrid fractal acoustic metamaterials for low-frequency sound absorber based on cross mixed micro-perforated panel mounted over the fractals structure cavity, Sci. Rep. **12**, 20444 (2022).

[16] R. Fleury, A. Khanikaev, and A. Alù, Floquet topological insulators for sound, Nat. Commun. **7**, 11744 (2016).

[17] Z. Zhang, Y. Tian, Y. Wang, S. Gao, Y. Cheng, X. Liu, and J. Christensen, Directional acoustic antennas based on valley-Hall topological insulators, Adv. Mater. **30**, 1803229 (2018).

[18] F. Zangeneh-Nejad and R. Fleury, Disorder-induced signal filtering with topological metamaterials, Adv. Mater. **32**, 2001034 (2020).

[19] T. Yamamoto, S. Maruyama, S. Nishiwaki, and M. Yoshimura, Topology design of multi-material soundproof structures including poroelastic media to minimize sound pressure levels, Comput. Methods Appl. Mech. Eng. **198**, 1439 (2009).

[20] Z. X. Xu, H. Gao, Y. J. Ding, J. Yang, B. Liang, and J. C. Cheng, Topology-optimized omnidirectional broadband acoustic ventilation barrier, Phys. Rev. Appl. **14**, 054016 (2020).

[21] C. Liu *et al.*, Three-dimensional soundproof acoustic metacage, Phys. Rev. Lett. **127**, 084301 (2021).

[22] C. K. Chiu, J. C. Y. Teo, A. P. Schnyder, and S. Ryu, Classification of topological quantum matter with symmetries, Rev. Mod. Phys. **88**, 035005 (2016).

[23] S. Zheng *et al.*, Observation of fractal higher-order topological states in acoustic metamaterials, Sci. Bull. **67**, 2069 (2022).

[24] Y. X. Xiao, G. Ma, Z. Q. Zhang, and C. T. Chan, Topological subspace-induced bound state in the continuum, Phys. Rev. Lett. **118**, 166803 (2017).

[25] G. Ma, M. Xiao, and C. T. Chan, Topological phases in acoustic and mechanical systems, Nat. Rev. Phys. **1**, 281 (2019).

[26] Y. Qi, C. Qiu, M. Xiao, H. He, M. Ke, and Z. Liu, Acoustic realization of quadrupole topological insulators, Phys. Rev. Lett. **124**, 206601 (2020).

[27] J. Asbóth, L. Oroszlány, and A. Pályi, A short course on topological insulators: Band-structure topology and edge states in one and two dimensions, Lecture Notes in Physics Vol. 919 (Springer, Switzerland, 2016).

[28] K. H. Matlack, M. Serra-Garcia, A. Palermo, S. D. Huber, and C. Daraio, Designing perturbative metamaterials from discrete models, Nat. Mater. **17**, 323 (2018).